Molten salt-confined pyrolysis towards carbon nanotube-backboned microporous carbon for high-energy-density and durable supercapacitor electrodes

Siliang Liu[1], Qichun Feng[1], Chao Zhang[1,*] and Tianxi Liu[1,2,*]

[1] State Key Laboratory for Modification of Chemical Fibers and Polymer Materials, College of Materials Science and Engineering, Innovation Center for Textile Science and Technology, Donghua University, Shanghai 201620, People's Republic of China
[2] Key Laboratory of Synthetic and Biological Colloids, Ministry of Education, School of Chemical and Material Engineering, Jiangnan University, Wuxi 214122, People's Republic of China

E-mail: czhang@dhu.edu.cn and txliu@fudan.edu.cn

CrossMark

Abstract

The development of a green and scalable construction of a three-dimensional (3D) hierarchically porous carbon as an electrode material for supercapacitors is promising but challenging. Herein, a carbon nanotube-backboned microporous carbon (CNT-MPC) was prepared by molten salt-confined pyrolysis, during which the salt eutectics simultaneously acted as a high-temperature reaction solvent and reusable template. Among the CNT-MPC, the CNT backbone provided a 3D conductive framework, whereas the MPC sheath possessed integrated mesopores and micropores as an efficient ion reservoir. As a result, the as-obtained CNT-MPC exhibited a high specific capacitance of 305.6 F g^{-1} at 1 A g^{-1}, high energy density of 20.5 W h kg^{-1} and excellent cyclic stability with no capacitance losses after 50 000 cycles. The molten-salt confined pyrolysis strategy therefore provides a low-cost, environmentally-friendly and readily industrialized route to develop a hierarchically porous carbon that is highly required for high-energy-density and durable supercapacitors.

Supplementary material for this article is available online

(Some figures may appear in colour only in the online journal)

1. Introduction

Supercapacitors have received extensive attention due to their unique features including high power density, long cycling life and low cost [1, 2]. However, their relatively low energy densities have largely limited the wide uses requiring both high energy and power density [3]. Rapid electron and ion diffusions are of great importance to achieve high-energy-density porous carbon electrodes [4]. To address this issue, the rational design and preparation of three-dimensional (3D) carbon materials with a hierarchical porosity are expected to significantly enhance both the energy and power density of porous carbon electrodes [5]. Among the various porous carbon, dendroid carbon materials are competitive in terms of their highly porous structure and 3D interconnected framework allowing an efficient and fast electron/ion transport [6, 7]. The practical applications of dendroid carbon materials in supercapacitor electrodes are urgent to address the following issues [8]. For instance, the production of these dendroid carbons should be avoided in high-cost and time-consuming supercritical CO_2

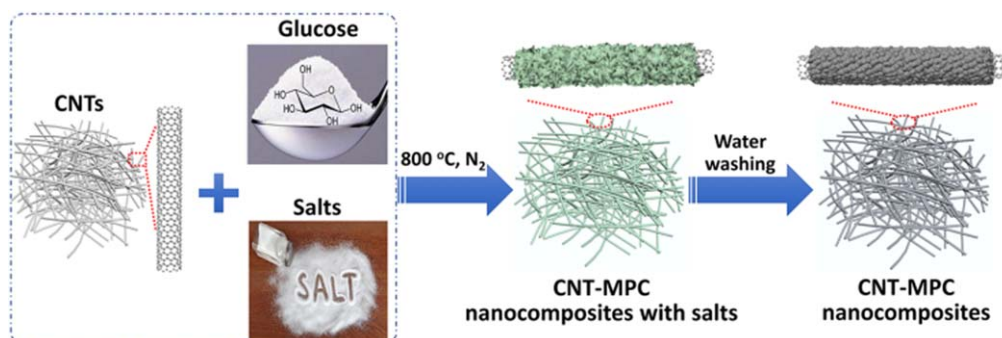* Authors to whom any correspondence should be addressed.

Figure 1. Schematic of the preparation procedure of the CNT-MPC in a molten-salt confined pyrolysis strategy.

drying processes [9, 10]. Besides, the electrical conductivity of dendroid carbon materials pyrolyzed at a high temperature is barely satisfactory at the expense of sacrificing their high surface area. Therefore, the rapid and large-scale production of dendroid carbon materials with a 3D conductive framework and tailored porosity in the usual synthesizing and drying conditions is attractive yet challenging [11].

Significant efforts have been focused on the preparation of dendroid carbon materials via hard- and soft-templating methods [12]. However, these traditional templating methods have obvious drawbacks such as the uses of toxic chemicals, the complicated operations to remove the templates, and the difficulties in precisely controlling the pore sizes [13]. An emerging salt-templating method provides a novel and environmental-friendly strategy for the preparation of dendroid carbon materials with high surface area and large pore volume [14, 15]. Compared with traditional templating methods, the salt eutectics used in the salt-templating were easily removed and recycled for the subsequent synthesis. Besides, the hierarchical porosity and microstructure evolution of carbon were tailored by simply employing different kinds of eutectics under mild pyrolysis conditions [16]. However, the effective conductive pathway is easily collapsed upon cycles due to the essence of interconnected carbon nanoparticles among the dendroid structures [17].

Herein, a molten salt-confined pyrolysis strategy is presented for preparing a carbon nanotube-backboned microporous carbon nanocomposite (CNT-MPC), among which a highly conductive CNT was closely enclosed by an MPC sheath, thus forming a 'carbon-in-carbon' coaxial structure. The CNT backbone provided a high electrical conductivity, while the MPC sheath possessed integrated mesopores and micropores as efficient ion reservoirs. The as-prepared CNT-MPC showed superior electrochemical capacitive performance including high specific capacitance, excellent rate performance and good cycling stability when evaluated as an electrode material for supercapacitors.

2. Experimental details

2.1. Synthesis of the CNT-MPC in a KCl/ZnCl$_2$ eutectic

A designed amount of CNTs, 1 g of glucose, and 10 g of KCl/ZnCl$_2$ eutectic (0.363/0.637 by weight) were ball-milled for 10 min. The mixture was transferred into a covered crucible and pyrolyzed at 800 °C for 1 h with a heating rate of 5 °C min^{-1}. Upon cooling, the products were washed with 5% HCl and water several times, respectively, to remove the impurities, and dried overnight in a vacuum at 60 °C. The CNT-MPC-1, CNT-MPC-2 and CNT-MPC-3 represent the CNT-MPC samples prepared with the addition of CNTs of 900, 300 and 100 mg, respectively. For comparison, neat MPCs were prepared similarly to the above procedure without the addition of CNTs.

2.2. Synthesis of the CNT-MPC in LiCl/ZnCl$_2$ and NaCl/ZnCl$_2$ eutectics

The CNT-MPC was prepared similarly to the above procedure for synthesizing the CNT-MPC-2, except using the LiCl/ZnCl$_2$ (0.093/0.907 by weight) and NaCl/ZnCl$_2$ (0.312/0.688 by weight) eutectics, and the products were denoted as CNT-MPC-LZ and CNT-MPC-NZ, respectively.

3. Result and discussion

Figure 1 exhibits the preparation procedures of the CNT-MPC. Pristine CNTs, glucose and KCl/ZnCl$_2$ eutectics were ball-milled and then pyrolyzed under a nitrogen atmosphere. The glucose is green and cheap biomass extracted from natural carbohydrates. Meanwhile, the glucose is a sustainable and low-cost precursor for pyrolysis synthesis of carbon materials with a high carbonization yield [18]. The thickness of the MPC sheath among the CNT-MPC was tailored by varying the initial weight ratio of CNTs and glucose. The kinds of eutectics also showed great influences on the porosity of the resultant CNT-MPC. The preparation procedure is convenient for large-scale production of CNT-MPC in one batch. The green and cheap biomass glucose is used as the precursor, and the pristine and commercially available CNTs (100 euros kg^{-1}) were directly used. The eutectics as a unique porogen promoted the formation of high-surface-area MPCs, which were simply devoted to a simple closed-loop process for the reproduction by being dissolved in water and subsequently evaporated [19]. The resultant CNT-MPC exhibited advantages when evaluated as an electrode material for supercapacitors. Especially, the highly conductive CNT
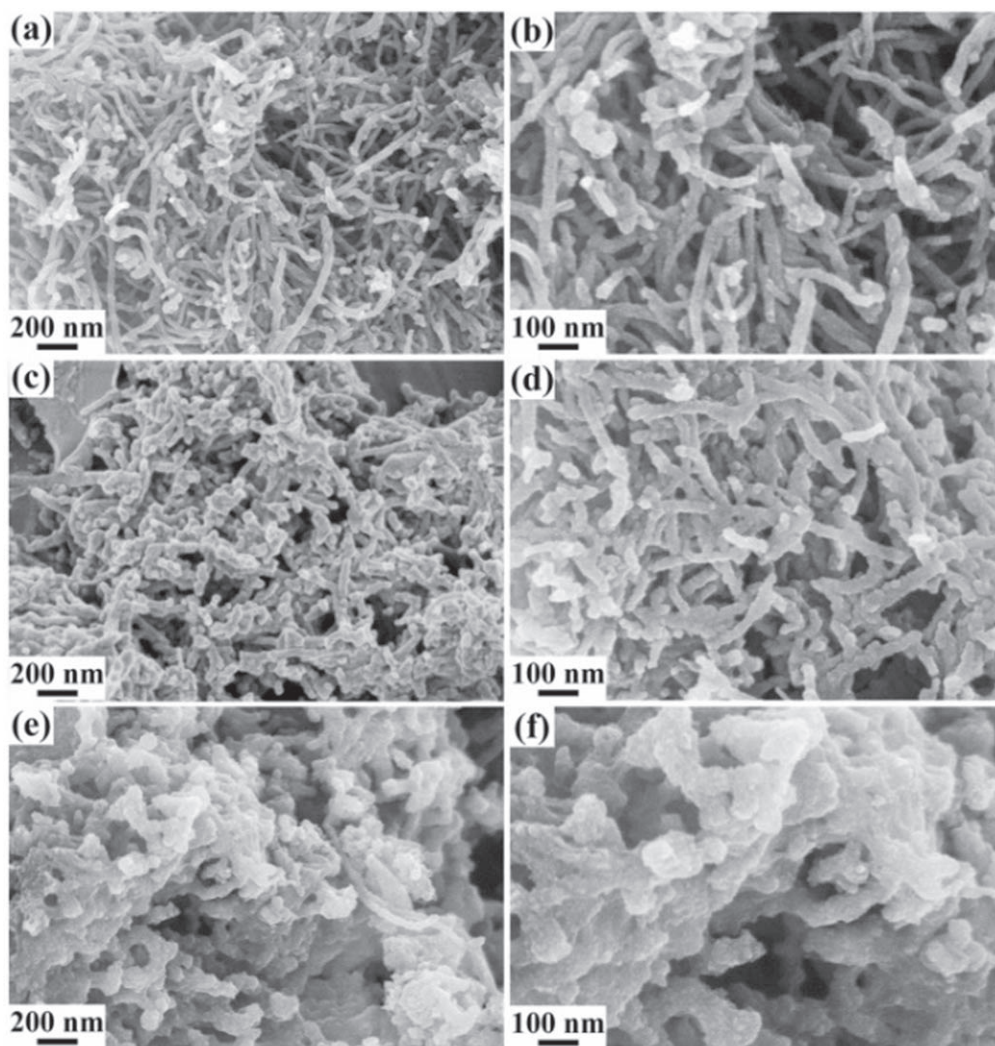
Figure 2. FESEM images of (a), (b) CNT-MPC-1, (c), (d) CNT-MPC-2 and (e), (f) CNT-MPC-3 at low and high magnifications, respectively.

framework provides fast electron transport, as well as relieving the volume expansion/contraction of MPCs during cycling [20]. The MPC sheath with high surface area and large pore volume provides an ion reservoir for efficient ion adsorption and desorption [21].

The morphologies of CNTs, MPCs and CNT-MPC were characterized by field-emission scanning electron microscopy (FESEM) and transmission electron microscopy (TEM). Long and curly CNTs were observed with an outer diameter of 20–30 nm and an average length larger than 10 μm, figures S1(a), (b) and S2(a), (b) (available online at stacks.iop.org/NANO/32/095605/mmedia). The MPCs with a 3D network of interconnected carbon nanoparticles were observed (figures S1(c), (d)). Closer TEM observations indicated that the 3D porous framework was composed of interconnected primary MPCs with an average particle size of 30 nm, and amorphous graphitic domains were observed within these irregularly shaped MPCs (figures S2(c), (d)). These primary MPCs were composed of tiny amorphous carbon with abundant micropores and mesopores, demonstrating their highly porous structure and easy transport of ions [22]. Owing

to their nanoscale sizes and hierarchical porosities, the primary MPCs showed the potentials to serve as sheath layers on the 3D CNT skeletons [23]. The morphological evolutions of CNT-MPC with different contents of MPCs were investigated. Figures 2(a)–(f) displayed FESEM images of the CNT-MPC with various thicknesses of decorated MPCs, and figures 3(a)–(f) indicated the coaxial structures of CNT-MPC. The average thicknesses of enwrapped MPCs were ∼4, 10, and 30 nm for the CNT-MPC-1, CNT-MPC-2 and CNT-MPC-3, respectively. The thicknesses of MPC increased with the increased feeding ratios of glucose to CNTs. The CNT-MPC-2 showed that the CNT skeletons were uniformly coated with MPCs, suggesting that the CNTs acted as a unique template and guided a nucleation growth of MPCs in the molten salt.

The electrochemical behaviors of CNT-MPC are closely related to its favorable micro/mesopore structures. The formation of carbon materials with significantly distinguished pore volumes and pore size distributions during the molten-salt pyrolysis depends on the kinds of eutectic salts, ascribed to their molten state with diverse clusters and percolation
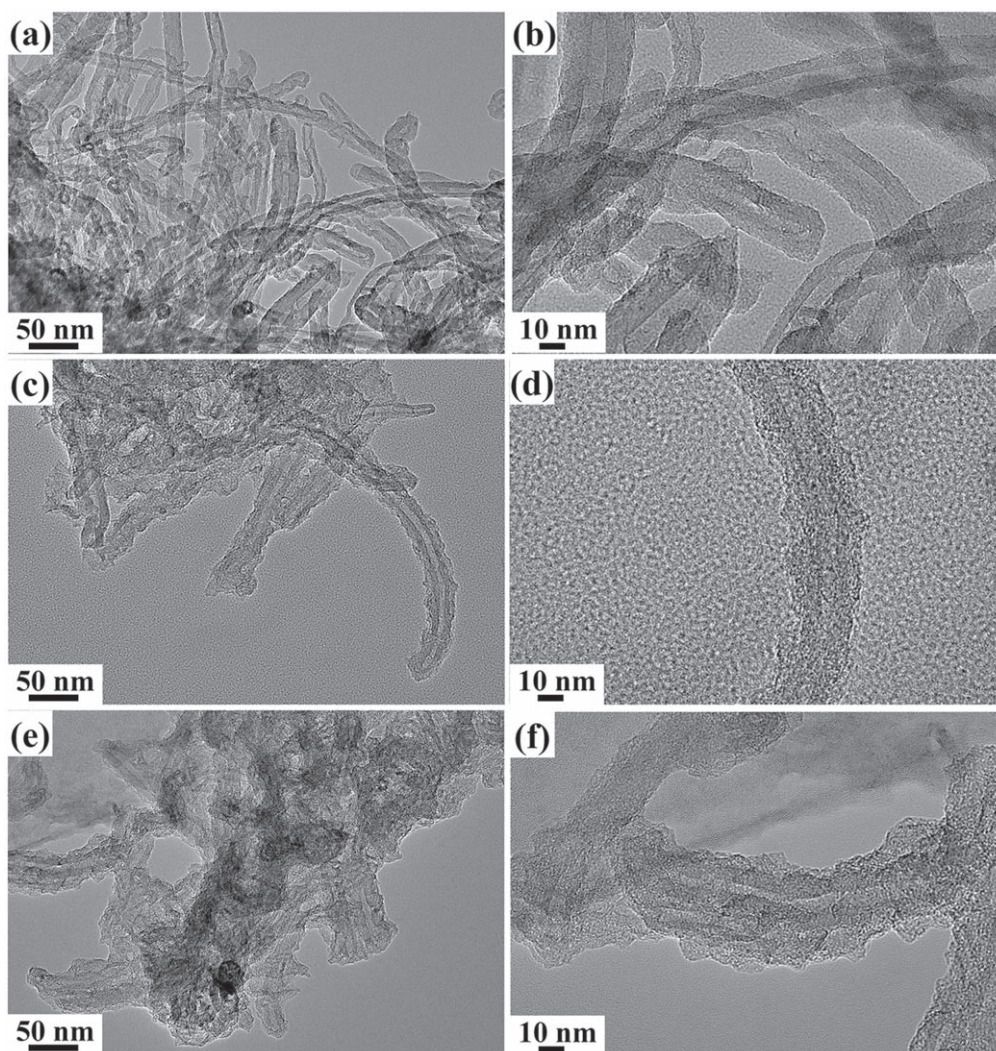
Figure 3. TEM images of (a), (b) CNT-MPC-1, (c), (d) CNT-MPC-2 and (e), (f) CNT-MPC-3 at low and high magnifications, respectively.

structures [16]. Therefore, different kinds of eutectic salts were used to tailor the pore structures of the resultant MPCs on CNT skeletons [24]. The CNT-MPC-LZ and CNT-MPC-NZ were designed and prepared in the LiCl/ZnCl$_2$ and NaCl/ZnCl$_2$ eutectic at a CNT/glucose feeding ratio similar to that of CNT-MPC-2. FESEM images of CNT-MPC-LZ (figures 4(a), (b)) and CNT-MPC-NZ (figures 4(c), (d)) were measured and compared with that of CNT-MPC-2 to investigate the structural evolutions derived from respective eutectics. For the CNT-MPC prepared in different eutectics, all the MPCs were strongly decorated on the surface of CNTs, indicating that CNTs were uniformly dispersed in all eutectic salts and guided the growth of MPCs. Compared with the relatively uneven yet smooth surface of MPCs within the CNT-MPC-LZ, the surface roughness of MPCs decorated on CNTs in the CNT-MPC-NZ and CNT-MPC-2 dramatically increased, suggesting the relatively low melting point and large salt clusters of eutectic salts resulted in the formation of the macro/mesopores instead of micropores among the carbon products [16]. Large mesopores as well as macropores resulted from unique salt-templating mechanisms by respective eutectics.

The compositions of CNT-MPC were characterized by x-ray diffraction (XRD) and Raman spectra analysis. Neat MPCs in figure 5(a) exhibited a weak and broad diffraction pattern at $2\theta = 24.5°$, which was assigned to (002) plane of carbon lattices, suggesting the nature of amorphous carbon of MPCs [25]. When CNTs are introduced to form the CNT-MPC, typical graphitic (002) diffraction pattern shifted to 25.6° and a low-intensity (100) diffraction pattern at 42.6° was observed, implying the existence of a highly graphitic carbon of CNTs and MPCs [26, 27]. No diffraction patterns ascribing to LiCl and KCl were observed from XRD results. Raman spectra were used to elucidate the graphitic structures of the CNT-MPC (figure 5(b)). The D-band at ~1350 cm^{-1} represented the A$_{1g}$ mode (structural defects) corresponding to disordered carbon structures [28]. The G-band at ~1580 cm^{-1} was associated with the E$_{2g}$ mode representing the C=C stretching in the graphitic carbon. Generally, the relative peak intensity ratio of the D band (I_D) to G band (I_G) represented graphitic degrees and graphitic crystallite sizes of carbon [29]. Compared with the I_D/I_G ratio of MPCs (0.95), the I_D/I_G ratios of CNT-MPC gradually decreased from 0.89 to 0.79 with increased CNT contents, indicating higher crystallized
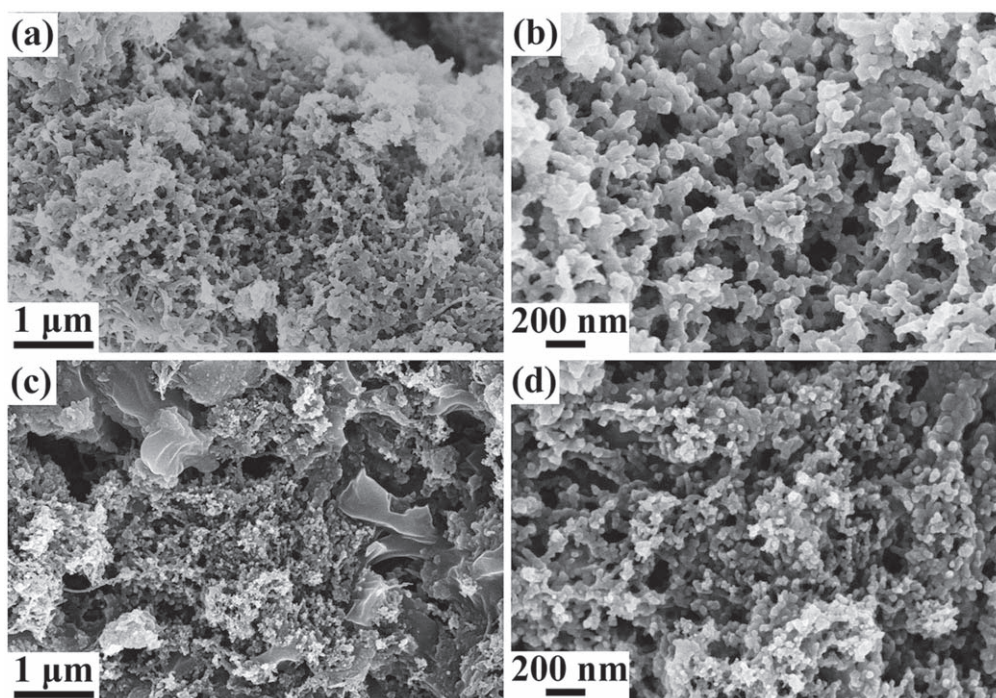
Figure 4. FESEM images of (a), (b) CNT-MPC-LZ, (c), (d) CNT-MPC-NZ at low and high magnifications, respectively.
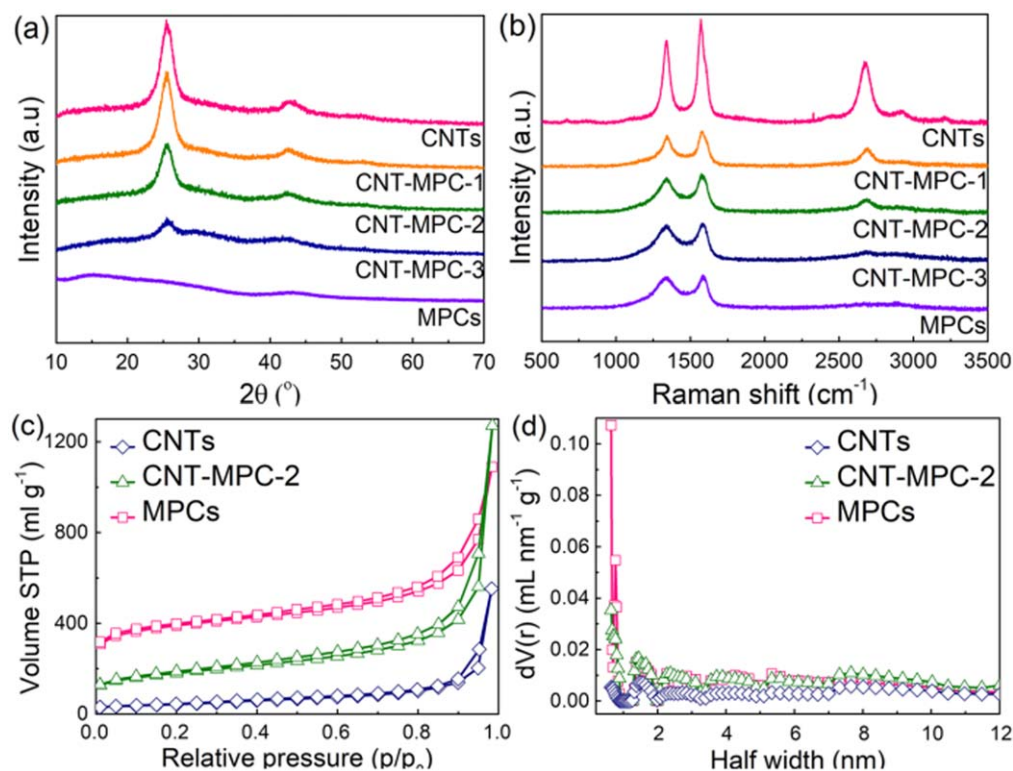

Figure 5. (a) XRD patterns and (b) Raman spectra of CNTs, CNT-MPC and MPCs. (c) Nitrogen adsorption–desorption isotherms and (d) pore size distributions of CNTs, CNT-MPC-2 and MPCs.

and larger graphitic domains due to the presence of CNTs [30]. Compared with neat MPCs, the appearances of sharp 2D peaks ($\sim$2643 cm^{-1}) of CNT-MPC were also features indicating a successful hybridization of CNTs in the nanocomposites.

The nitrogen adsorption–desorption isotherms and pore size distributions of CNTs, CNT-MPC and MPCs were measured in figures 5(c), (d) and S3(a), (b). The first nitrogen-uptake steps at relatively low pressure ($p/p_0 < 0.2$) and small hysteresis at p/p_0 from 0.2 to 0.8 in the CNT-MPC and MPCs

demonstrated the presences of micropores and mesopores in these samples [31]. The steep increases of the CNTs, CNT-MPC and MPCs at a high relative pressure ($p/p_0 > 0.9$) are attributed to macropores derived from interstitial voids between particles. The pore size distributions of CNT-MPC and MPCs with humps from 0.7 to 12 nm revealed the presence of micropores and good degrees of mesoporosity. The values of the specific surface area and pore volumes of CNTs, CNT-MPC and MPCs were calculated (table S1). With increased contents of MPCs within the CNT-MPC, the Brunauer–Emmett–Teller (BET) surface areas increased from 257 (CNT-MPC-1) to 832 m^2 g^{-1} (CNT-MPC-3), meanwhile, the pore volumes increased from 0.59 to 1.18 ml, indicating that the surface area and meso/micropore volume were simply controlled by altering mass ratios of CNTs and glucose for the synthesis of CNT-MPC. Compared with CNT-MPC-2, the isotherm of CNT-MPC-LZ derived from $LiCl/ZnCl_2$ eutectics showed the hysteresis with defined plateau region at p/p_0 from 0.2 to 0.8, indicating the microporous structure among the sample, meanwhile, the isotherm of CNT-MPC-NZ derived from $NaCl/ZnCl_2$ eutectics showed a further uptake of nitrogen in the medium relative pressure region as well as a small hysteresis, reflecting a combined contribution of micro/mesopores (figures S3(c), (d)) [32]. Although the BET surface area did not change too much when the eutectics changed, great changes in pore volumes and pore size distributions were observed. The proportions of mesopores among the CNT-MPC-NZ (69%) and CNT-MPC-LZ (50%) greatly decreased compared with that of CNT-MPC-2 (83%). The CNT-MPC-2 had almost two times larger pore volume than those of CNT-MPC-NZ and CNT-MPC-LZ. More mesopores within the composites contributed to lower ion diffusion resistances, and while the micropores played an important role in enlarging the electric double-layer surfaces and therefore boosting the specific capacitances. Therefore, the unique hierarchical porosities endowed CNT-MPC-2 with high capacitive values and excellent rate performances [33].

The elemental contents of carbon, hydrogen and oxygen within CNTs, CNT-MPC and MPCs were measured by an elemental analysis using a combustion method (figure S4). The C/O weight ratios of CNTs, CNT-MPC-1, CNT-MPC-2, CNT-MPC-3 and MPCs were calculated to be 54.4, 19.4, 6.8, 5.6 and 4.2, respectively. The efficient oxygen doping within the carbon frameworks contributed to generating additional pseudocapacitances with an efficient electron transfer. All the CNT-MPC exhibited high graphitization degrees with carbon contents larger than 83 wt%. The theoretical carbonization yield of converting glucose into carbon materials is ∼32 wt% in the eutectics, and the C/O weight ratios of CNTs and MPCs are measured as 54.4 and 4.2, respectively. The theoretical C/O weight ratios of the CNT-MPC-1, CNT-MPC-2 and CNT-MPC-3 are calculated as 40.1, 28.3 and 16.1, respectively, which are larger than the actual C/O weight ratios of the as-prepared CNT-MPC. The result indicates that the CNTs greatly increase the graphitization degree of the decorated MPCs.

The electrical conductivity of CNTs, CNT-MPC and MPCs were characterized by a four-probe method, and the electrical conductivities were summarized in table S2. According to the percolation theory, an electrical percolation network is achieved by using 1D conductive nanofillers compared with 3D MPCs, and the electrical conductivities of the CNT-MPC increased from 0.83 to 1.8 S cm^{-1} with increasing content of CNTs within the CNT-MPC, indicating that highly conductive CNT skeletons were very helpful to improve the electrical conductivity of the nanocomposites. When evaluated as an electrode material, the electrons could be easily and continuously transported through the CNT-MPC, in which good interfacial interactions and low interfacial resistances were simultaneously achieved due to the formation of efficient junctions between individual CNT-MPC structures.

Elemental composition and chemical states of the atoms within CNTs, CNT-MPC and MPCs were measured by x-ray photoelectron spectroscopy (XPS) [34]. The typical XPS wide scan spectra of MPCs, CNTs and CNT-MPC were measured in figure 6(a). The spectra of each sample exhibited peaks for C1s and O1s, indicating the presence of carbon and oxygen [35, 36]. There were no obvious Zn, K and Cl elemental peaks in the XPS spectra, indicating that the molten salts were completely removed after water washing. All the samples had low oxygen contents and high C/O ratios, consistent with the results of elemental analysis. The high-resolution C1s XPS spectra of CNTs, CNT-MPC and MPCs were deconvoluted into four peaks, corresponding to different types of carbon species (figures 6(b)–(f)). The peak at 284.5eV corresponded to the sp^2-hybridized carbon atoms (C=C), and the peaks at 285.7, 286.5, and 287.7eV are assigned to C–OH, C=O, O–C=O groups, respectively [37, 38]. The oxygen-containing functional groups in electrode materials facilitated electrolyte infiltrations. With an increased glucose/CNT ratio, the content of C=C groups among total carbon species decreased from 89.7% (CNTs) to 64.1% (MPCs), indicating that the proportion of MPCs within the CNT-MPC was strongly influenced by the precursor compositions.

Cyclic voltammetry (CV) and galvanostatic charge/discharge (GCD) measurements were used to investigate the electrochemical performance of CNT-MPC. CV curves of all the electrodes presented nearly rectangular shapes and symmetric characteristics, indicating an ideal electric double-layer capacitance and fast adsorption/desorption rate. Figure 7(a) showed CV curves of the CNT-MPC, CNTs and MPCs at a scan rate of 10 mV s^{-1} in a 6 M KOH electrolyte, among which the CNT-MPC-2 electrode exhibited a high specific capacitance and excellent electrochemical performance. The effects of pore structures of MPC sheath among the CNT-MPC on the electrochemical performance were investigated. Figure 7(b) exhibits the CV curves of CNT-MPC-2, CNT-MPC-LZ and CNT-MPC-NZ. The CNT-MPC-2 electrode exhibited a higher specific capacitance compared with those of CNT-MPC-LZ and CNT-MPC-NZ, indicating the CNT-MPC-2 exhibited a low ion transfer resistance during the charging/discharging due to its large surface area and optimized micro/mesoporous structure [39]. The CNT-MPC-2 exhibited a nearly rectangular shape even at a high sweep rate
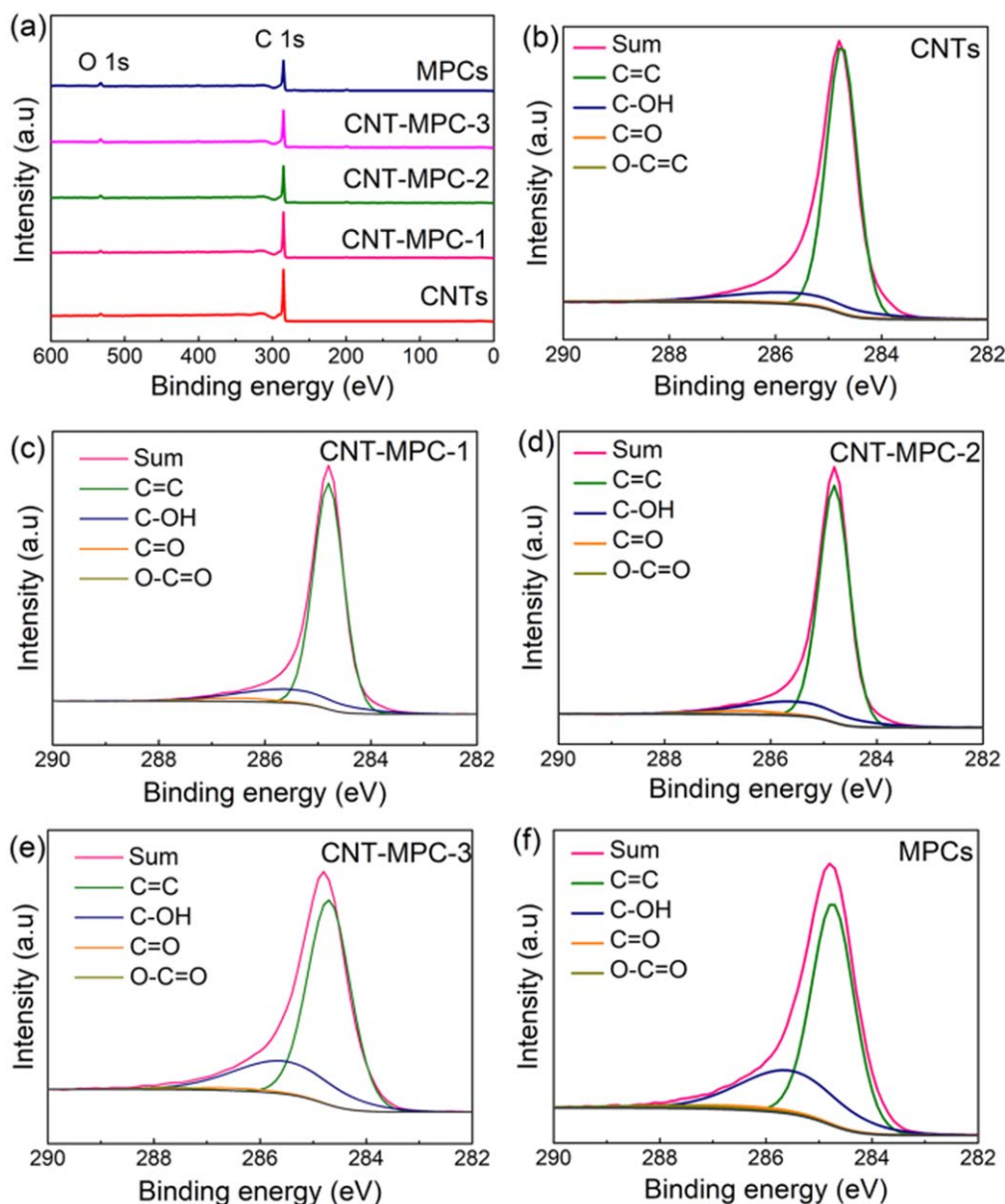
Figure 6. (a) XPS survey spectra of CNTs, CNT-MPC and MPCs. C1s XPS spectra of (b) CNTs, (c) CNT-MPC-1, (d) CNT-MPC-2, (e) CNT-MPC-3 and (f) MPCs.

of 200 mV s^{-1} (figure S5(a)), demonstrating the fast ion transport among the electrode. The extremely fast current–voltage responses were ascribed to the unique skeleton/sheath structure of CNT-MPC-2. The GCD curves of CNT-MPC-2 were further measured at a current density ranging from 2 to 20 A g^{-1} (figure S5(b)). The isosceles triangular shapes without obvious *iR* drops among the charge/discharge curves of CNT-MPC-2 were observed, suggesting a fast electric transport due to the highly conductive CNT skeletons. The closely anchored MPCs on CNT skeletons also improved the interfacial interaction between CNT skeleton and MPC sheath, greatly shortening the diffusion and migration pathways for ions and electrons during rapid charge/discharge processes [40].

The specific capacitances of CNT-MPC, CNTs and MPCs at various scan rates were calculated from GCD curves

(figure 7(c)). Compared with MPCs (98 F g^{-1}) and CNTs (124 F g^{-1}), the CNT-MPC-2 performed a high specific capacitance of 306 F g^{-1} at 1 A g^{-1}, indicating its excellent electrochemically accessible surface area. This result further explained that the CNTs served as an ideal conductive framework while decorated MPCs acted as an ion reservoir contributing to large capacitances [41]. The lower capacitances of CNT-MPC-1 were ascribed to a rare ion reservoir due to lower MPC content within the CNT-MPC. On the contrary, the low capacitances of CNT-MPC-3 especially at a large current density were attributed to low electrical conductivity with an insufficient conductive pathway. The specific capacitance of CNT-MPC-2 only decreased ∼26% when the current density increased from 1 to 20 A g^{-1}. In comparison, the specific capacitances of MPCs and CNTs decreased ∼39% and 45%, respectively. Moreover, the CNT-MPC-2 delivered a high
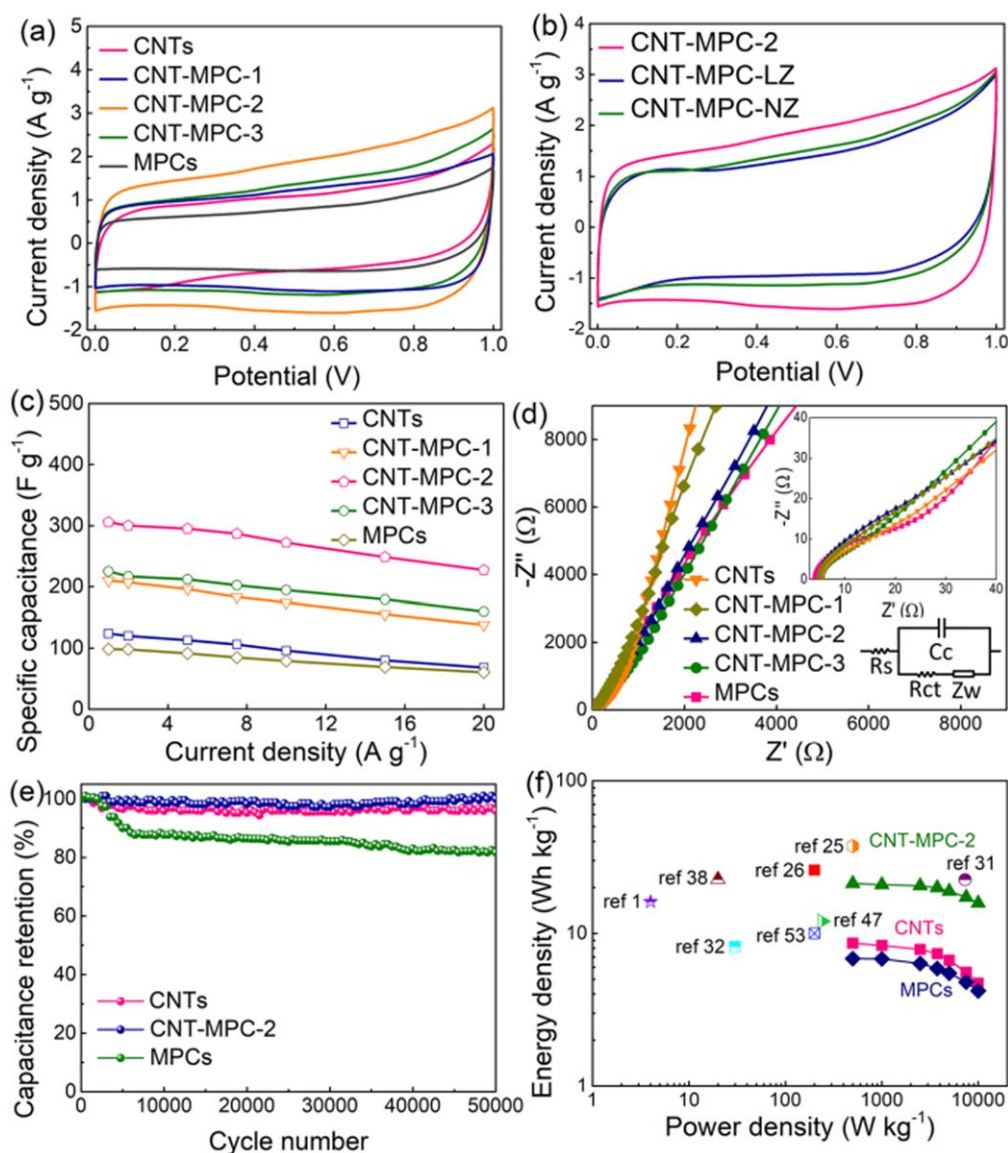
Figure 7. (a) CV curves of CNTs, CNT-MPC and MPCs at 10 mV s^{-1}. (b) CV curves of CNT-MPC-2, CNT-MPC-LZ and CNT-MPC-NZ at 10 mV s^{-1}. (c) Specific capacitances of CNTs, CNT-MPC and MPCs at various current densities. (d) Nyquist plots of CNTs, CNT-MPC and MPCs. Inset of (d) showing the enlarged high-frequency region and the equivalent circuit. (e) Cyclic stability of CNTs, CNT-MPC-2 and MPCs for 50 000 cycles. (f) Ragone plots of supercapacitor devices with CNTs, CNT-MPC-2, MPCs and other carbon electrodes in the literature.

specific capacitance of 227 F g^{-1} at a high current density of 20 A g^{-1}, almost three and four times larger than those of neat CNTs (68 F g^{-1}) and MPCs (60.5 F g^{-1}), respectively. The specific capacitances of CNT-MPC-LZ and CNT-MPC-NZ at various scan rates were calculated (figure S6(a)). Compared with CNT-MPC-LZ (199 F g^{-1}) and CNT-MPC-NZ (228 F g^{-1}), the CNT-MPC-2 performed a high specific capacitance at 1 A g^{-1}. The specific capacitances of CNT-MPC-LZ and CNT-MPC-NZ decreased by 30% and 32%, respectively, still larger than those of CNT-MPC-2, with the current density ranging from 1 to 20 A g^{-1}. The excellent rate capacitances of CNT-MPC-2 were ascribed to lower ion exchange resistance, more rapid electrolyte penetration and better electrical conductivity, benefiting from the 3D

interconnected hierarchical porosity and conductivity framework. The abundant micro/mesopores derived from the MPC sheath played essential roles for optimized electrical double-layer surfaces, efficiently enlarging the capacitances due to short immigration distances for ions. In contrast to other porogen salts, KCl/ZnCl$_2$ eutectics efficiently optimized interconnected mesopores and therefore provided abundant mesopore volume [19]. The electrochemical parameters of CNT-MPC-2 were compared with various CNT/porous carbon electrodes in the previous literature and summarized in table 1. In contrast to various CNT/porous carbon reported before, the CNT-MPC-2 showed a competitive electrochemical capacitive behavior. Considering the tunable micro/mesopore structure, excellent electrical conductivity and environmental-friendly

Table 1. Summary of electrochemical parameters of the CNT-MPC with CNT-based composites in the literature.

Electrode materials	Specific capacitances	Electrolytes	References
Activated carbon/CNT hybrid	140 F g^{-1}, 5 mV s^{-1}	Basic	[42]
Biomass carbon/CNT hybrid	111 F g^{-1}, 10 mA cm^{-2}	Acidic	[43]
N-doped porous carbon/CNT hybrid	262 F g^{-1}, 0.5 A g^{-1}	Acidic	[44]
N-doped carbon polyhedra/CNT hybrid	308 F g^{-1}, 5 mV s^{-1}	Acidic	[45]
B/N-doped CNT/CNS hybrid	389 F g^{-1}, 1 A g^{-1}	Basic	[46]
Activated carbon-wrapped CNT film	110 F g^{-1}, 5 mV s^{-1}	Basic	[47]
Phosphated CNT/carbon composite	160 F g^{-1}, 0.1 A g^{-1}	Basic	[48]
Activated carbon/CNT composite film	270.9 F g^{-1}, 10 mV s^{-1}	Basic	[49]
Carbon/CNT composite microelectrode	6 mF cm^{-2}, 10 mV s^{-1}	Acidic	[50]
CNT@N-doped carbon layer composite	205 F g^{-1}, 20 mV s^{-1}	Basic	[51]
P-doped carbon/CNT monolith	220 F g^{-1}, 300 mA g^{-1}	Acidic	[40]
ZIF8 derived carbon/CNT composite	293.4 F g^{-1}, 5 mV s^{-1}	Acidic	[52]
CNT@mesoporous carbon composite	538 F g^{-1}, 1 A g^{-1}	Acidic	[53]
N-doped carbon/CNT composite	56 F g^{-1}, 2 mV s^{-1}	Acidic	[54]
Activated carbon-coated CNT composite	103 F g^{-1}, 2 mV s^{-1}	Neutral	[1]
CNT/N-doped porous carbon monolith	216 F g^{-1}, 10 mV s^{-1}	Acidic	[55]
CNT-MPC-2	**305.6 F g^{-1}, 1 A g^{-1}**	**Basic**	**This work**

synthesis route, this study therefore demonstrated great potentials for fabricating promising carbon electrode materials for supercapacitors.

To further understand the electrochemical performances of the CNT-MPC, electrochemical impedance spectroscopy was used to investigate ion diffusion kinetics during electrochemical processes. Nyquist plots of CNTs, CNT-MPC and MPCs showed nearly straight lines in low-frequency regions, indicating their ideal electric double layer behaviors (figure 7(d)). Compared with MPCs and CNT-MPC, the Nyquist plot of CNTs was closer to the *y*-axis, resulting from a highly graphitic structure and excellent electrical conductivity of neat CNTs. The Nyquist plots of all the electrodes matched up with Randle's equivalent circuit (Inset of figure 7(d)). In the high-frequency region, there were no obvious semicircles, suggesting the low charge-transfer resistance (R_{ct}) and ion diffusion resistances (Z_w) among the electrodes of CNTs, CNT-MPC and MPCs [56]. Also, the CNT-MPC performed decreased equivalent series resistances (R_s) compared with that of neat MPCs and CNTs, indicating the relatively low internal resistances, balanced micro/mesoporosity and fast ion penetration within the CNT-MPC electrodes.

Cycling stabilities of CNTs, CNT-MPC and MPCs were evaluated by repeating the GCD measurements at 10 A g^{-1} (figure 7(e)). The CNT-MPC-2 showed excellent cycling stability with no capacitance losses after 50 000 cycles, compared with that of CNTs (96.2%) and MPCs (82.1%), respectively. The excellent cycling stability of CNT-MPC-2 indicated that MPCs with the CNT skeletons effectively alleviated volume changes during cycling [57]. Besides, the CNT skeleton also offered a unique 3D framework with high electrical conductivity to overcome the drawbacks of efficient connections between randomly scattered MPCs [58].

The Ragone plots corresponding to the energy density and power density of as-assembled symmetric supercapacitors were calculated. When the power density increased from 0.5 to 5 kW kg^{-1}, the resulting energy densities of the supercapacitor

device with CNT-MPC-2 decreased only 11% (from 21.2 to 18.9 W h kg^{-1}), smaller than those of CNT-MPC-1 (18%) and CNT-MPC-3 (14%) (figure S6(b)). The Ragone plot of CNT-MPC-2 was further compared with neat CNTs, MPCs as well as CNT/porous carbon composites in the literature (figure 7(f)). The supercapacitor device with CNT-MPC-2 electrodes displayed an energy density of 20.5 W h kg^{-1} at a power density of 2 kW kg^{-1}, much larger than those of CNTs (7.8 W h kg^{-1}) and MPCs (6.3 W h kg^{-1}). The energy density of the supercapacitor device with CNT-MPC-2 electrodes outperformed most of the CNT/porous carbon composites in the literature, indicating the skeleton/sheath structured CNT-MPC with a hierarchical porosity and excellent electrical conductivity efficiently boosted the energy storage [59]. Although very few CNT/porous carbon composite electrodes with an even larger energy density were reported compared with CNT-MPC-2, their relatively larger energy densities were only realized by using complicated synthetic routes or introducing transition-metal compounds suffering sacrifices of cycling stability [53, 60].

4. Conclusion

In summary, the CNT-MPC nanocomposites with a hierarchical porosity and 3D conductive framework were prepared in an extremely simple, environmentally friendly and easily scalable molten salt-confined pyrolysis strategy. Among the as-prepared CNT-MPC nanocomposites, the CNT backbone is beneficial to the formation of a 3D conductive framework, while the MPC sheath helps to provide an efficient ion reservoir. Compared with the eutectics of LiCl/ZnCl$_2$ and NaCl/ZnCl$_2$, the CNT-MPC-2 that was prepared in the KCl/ZnCl$_2$ eutectics showed high specific capacitance of 305.6 F g^{-1} at 1 A g^{-1}, high energy density of 20.5 W h kg^{-1} and excellent cyclic stability with no capacitance losses after 50 000 cycles. The proof-of-concept study

of the fabrication of hierarchically porous carbon fully demonstrates its potentials as promising electrode materials for high-energy-density supercapacitors.

Acknowledgments

ORCID iDs

Chao Zhang ⓘ https://orcid.org/0000-0003-1255-7183
Tianxi Liu ⓘ https://orcid.org/0000-0002-5592-7386

References

[1] Shi K, Ren M and Zhitomirsky I 2014 Activated carbon-coated carbon nanotubes for energy storage in supercapacitors and capacitive water purification *ACS Sustain. Chem. Eng.* **2** 1289–98

[2] Banda H, Perie S, Daffos B, Taberna P, Dubois L, Crosnier O, Simon P, Lee D, De Paepe G and Duclairoir F 2019 Sparsely pillared graphene materials for high-performance supercapacitors: improving ion transport and storage capacity *ACS Nano* **13** 1443–53

[3] Borchardt L, Leistenschneider D, Haase J and Dvoyashkin M 2018 Revising the concept of pore hierarchy for ionic transport in carbon materials for supercapacitors *Adv. Energy Mater.* **8** 1800892

[4] He Y, Zhuang X, Lei C, Lei L, Hou Y, Mai Y and Feng X 2019 Porous carbon nanosheets: synthetic strategies and electrochemical energy related applications *Nano Today* **24** 103–19

[5] Li Z, Gadipelli S, Yang Y and Guo Z 2017 Design of 3D graphene-oxide spheres and their derived hierarchical porous structures for high performance supercapacitors *Small* **13** 1702474

[6] Li Y, Samad Y, Polychronopoulou K and Liao K 2015 Lightweight and highly conductive aerogel-like carbon from sugarcane with superior mechanical and emi shielding properties *ACS Sustain. Chem. Eng.* **3** 1419–27

[7] Cai G, Zhang W, Jiao L, Yu S and Jiang H 2017 Template-directed growth of well-aligned MOF arrays and derived self-supporting electrodes for water splitting *Chem* **2** 791–802

[8] Ding M, Bannuru K, Wang Y, Guo L, Baji A and Yang H 2018 Free-standing electrodes derived from metal-organic frameworks/nanofibers hybrids for membrane capacitive deionization *Adv. Mater. Technol.* **3** 1800135

[9] Chang A, Zhang C, Yu Y, Yu Y and Zhang B 2018 Plasma-assisted synthesis of NiSe₂ ultrathin porous nanosheets with selenium vacancies for supercapacitor *ACS Appl. Mater. Interfaces* **10** 41861–5

[10] Deng Y, Xie Y, Zou K and Ji X 2016 Review on recent advances in nitrogen-doped carbons: preparations and applications in supercapacitors *J. Mater. Chem.* A **4** 1144–73

[11] Su C, Pei C, Wu B, Qian J and Tan Y 2017 Highly doped carbon nanobelts with ultrahigh nitrogen content as high-performance supercapacitor materials *Small* **13** 1700834

[12] Fellinger T, White R, Titirici M and Antonietti M 2012 Borax-mediated formation of carbon aerogels from glucose *Adv. Funct. Mater.* **22** 3254–60

[13] Yan Y, Yang H, Zhang F, Tu B and Zhao D 2006 Surfactant-templated synthesis of 1d single-crystalline polymer nanostructures *Small* **2** 517–21

[14] Dash A, Vassen R, Guillon O and Gonzalez-Julian J 2019 Molten salt shielded synthesis of oxidation prone materials in air *Nat. Mater.* **18** 465–70

[15] Fan E, Li L, Lin J, Wu J, Yang J, Wu F and Chen R 2019 Low-temperature molten-salt-assisted recovery of valuable metals from spent lithium-ion batteries *ACS Sustain. Chem. Eng.* **7** 16144–50

[16] Liu X, Fechler N and Antonietti M 2013 Salt melt synthesis of ceramics, semiconductors and carbon nanostructures *Chem. Soc. Rev.* **42** 8237–65

[17] Wickramaratne N, Xu J, Wang M, Zhu L, Dai L and Jaroniec M 2014 Nitrogen enriched porous carbon spheres: attractive materials for supercapacitor electrodes and CO₂ adsorption *Chem. Mater.* **26** 2820–8

[18] Gao Z, Zhang Y, Song N and Li X 2016 Biomass-derived renewable carbon materials for electrochemical energy storage *Mater. Res. Lett.* **5** 69–88

[19] Zhao Y, Liu J, Hu Y, Cheng H, Hu C, Jiang C, Jiang L, Cao A and Qu L 2013 Highly compression-tolerant supercapacitor based on polypyrrole-mediated graphene foam electrodes *Adv. Mater.* **25** 591–5

[20] Jayaramulu K, Dubal D, Nagar B, Ranc V, Tomanec O, Petr M, Datta K, Zboril R, Gomez-Romero P and Fischer R 2018 Ultrathin hierarchical porous carbon nanosheets for high-performance supercapacitors and redox electrolyte energy storage *Adv. Mater.* **30** 1705789

[21] Kale V *et al* 2018 Microporosity-controlled synthesis of heteroatom codoped carbon nanocages by wrap-bake-sublime approach for flexible all-solid-state-supercapacitors *Adv. Funct. Mater.* **28** 1803786

[22] Wang H, Yang H, Wang D, Cheng D, Deng T, Liu H, Zhang H, Zhang W and Zheng W 2019 Designing chemical bonds between active materials and current collectors for packaging a high-performance supercapacitor *Nanotechnology* **31** 105402

[23] Lu X, Yu M, Zhai T, Wang G, Xie S, Liu T, Liang C, Tong Y and Li Y 2013 High energy density asymmetric quasi-solid-state supercapacitor based on porous vanadium nitride nanowire anode *Nano Lett.* **13** 2628–33

[24] Cao L, Liu L, Chen X, Huang M, Wang X and Long J 2020 Scalable syntheses of three-dimensional graphene nanoribbon aerogels from bacterial cellulose for supercapacitors *Nanotechnology* **31** 095403

[25] Chen Y, Liu Y, Dong Y, Xia Y, Hung C, Liu L, Bi W and Li W 2020 Synthesis of sandwich-like graphene@mesoporous nitrogen-doped carbon nanosheets for application in high-performance supercapacitors *Nanotechnology* **31** 024001

[26] Yan S, Tang C, Zhang H, Yang Z, Wang X, Zhang C and Liu S 2020 Free-standing cross-linked activated carbon nanofibers with nitrogen functionality for high-performance supercapacitors *Nanotechnology* **31** 025402

[27] Perera Jayawickramage R, Balkus K and Ferraris J 2019 Binder free carbon nanofiber electrodes derived from polyacrylonitrile-lignin blends for high performance supercapacitors *Nanotechnology* **30** 355402

[28] Cho S, Jung I, Zhang L, Yoo S, Won J, Jung S, Liu L and Park S 2019 Synthesis of edge-rich vertical multilayer graphene nanotube arrays towards high-performance supercapacitors *Nanotechnology* **30** 425401

[29] Wang D, Li F, Chen Z, Lu G and Cheng H 2008 Synthesis and electrochemical property of boron-doped mesoporous carbon in supercapacitor *Chem. Mater.* **20** 7195–200

[30] Li H, Gong Y, Fu C, Zhou H, Yang W, Guo M, Li M and Kuang Y 2017 A novel method to prepare a nanotubes@mesoporous carbon composite material based on waste biomass and its electrochemical performance *J. Mater. Chem.* A **5** 3875–87

[31] Kim T, Jung G, Yoo S, Suh K and Ruoff R 2013 Activated graphene-based carbons as supercapacitor electrodes with macro- and mesopores *ACS Nano* **7** 6899–905

[32] Guo H, Zhou J, Li Q, Li Y, Zong W, Zhu J, Xu J, Zhang C and Liu T 2020 Emerging dual-channel transition-metal-oxide quasiaerogels by self-embedded templating *Adv. Funct. Mater.* **30** 2000024

[33] Guo H, Feng Q, Xu K, Xu J, Zhu J, Zhang C and Liu T 2019 Self-templated conversion of metallogel into heterostructured tmp@carbon quasiaerogels boosting bifunctional electrocatalysis *Adv. Funct. Mater.* **29** 1903660

[34] Niu Z *et al* 2012 A 'skeleton/skin' strategy for preparing ultrathin free-standing single-walled carbon nanotube/polyaniline films for high performance supercapacitor electrodes *Energy Environ. Sci.* **5** 8726–33

[35] Qiu L, Liu J, Chang S, Wu Y and Li D 2012 Biomimetic superelastic graphene-based cellular monoliths *Nat. Commun.* **3** 1241

[36] Chen S, Zheng Y, Zhang B, Feng Y, Zhu J, Xu J, Zhang C, Feng W and Liu T 2019 Cobalt, nitrogen-doped porous carbon nanosheet-assembled flowers from metal-coordinated covalent organic polymers for efficient oxygen reduction *ACS Appl. Mater. Interfaces* **11** 1384–93

[37] Liu S, Xu J, Zhu J, Chang Y, Wang H, Liu Z, Xu Y, Zhang C and Liu T 2017 Leaf-inspired interwoven carbon nanosheet/nanotube homostructures for supercapacitors with high energy and power densities *J. Mater. Chem.* A **5** 19997–20004

[38] Guo H, Feng Q, Zhu J, Xu J, Li Q, Liu S, Xu K, Zhang C and Liu T 2019 Cobalt nanoparticle-embedded nitrogen-doped carbon/carbon nanotube frameworks derived from a metal–organic framework for tri-functional orr, oer and her electrocatalysis *J. Mater. Chem.* A **7** 3664–72

[39] Li P, Li H, Han D, Shang T, Deng Y, Tao Y, Lv W and Yang Q 2019 Packing activated carbons into dense graphene network by capillarity for high volumetric performance supercapacitors *Adv. Sci.* **6** 1802355

[40] Patiño J, López-Salas N, Gutiérrez M, Carriazo D, Ferrer M and del Monte F 2016 Phosphorus-doped carbon–carbon nanotube hierarchical monoliths as true three-dimensional electrodes in supercapacitor cells *J. Mater. Chem.* A **4** 1251–63

[41] Wang Q, Yan J, Wang Y, Wei T, Zhang M, Jing X and Fan Z 2014 Three-dimensional flower-like and hierarchical porous carbon materials as high-rate performance electrodes for supercapacitors *Carbon* **67** 119–27

[42] Geng X, Li L and Li F 2015 Carbon nanotubes/activated carbon hybrid with ultrahigh surface area for electrochemical capacitors *Electrochim. Acta* **168** 25–31

[43] Dolah B, Deraman M, Othman M, Farma R, Taer E, Awitdrus A, Basri N, Talib I, Omar R and Nor N 2014 A method to produce binderless supercapacitor electrode monoliths from biomass carbon and carbon nanotubes *Mater. Res. Bull.* **60** 10–9

[44] Kim K and Park S 2012 Synthesis and high electrochemical capacitance of N-doped microporous carbon/carbon nanotubes for supercapacitor *J. Electroanal. Chem.* **673** 58–64

[45] Xu X, Wang M, Liu Y, Li Y, Lu T and Pan L 2016 *In situ* construction of carbon nanotubes/nitrogen-doped carbon

polyhedra hybrids for supercapacitors *Energy Storage Mater.* **5** 132–8

[46] Zhu S, Li J, Li Q, He C, Liu E, He F, Shi C and Zhao N 2016 Space-confined synthesis of three-dimensional boron/nitrogen-doped carbon nanotubes/carbon nanosheets line-in-wall hybrids and their electrochemical energy storage applications *Electrochim. Acta* **212** 621–9

[47] Chen H, Di J, Jin Y, Chen M, Tian J and Li Q 2013 Active carbon wrapped carbon nanotube buckypaper for the electrode of electrochemical supercapacitors *J. Power Sources* **237** 325–31

[48] Fan X, Yu C, Ling Z, Yang J and Qiu J 2013 Hydrothermal synthesis of phosphate-functionalized carbon nanotube-containing carbon composites for supercapacitors with highly stable performance *ACS Appl. Mater. Interfaces* **5** 2104–10

[49] Xu G, Zheng C, Zhang Q, Huang J, Zhao M, Nie J, Wang X and Wei F 2011 Binder-free activated carbon/carbon nanotube paper electrodes for use in supercapacitors *Nano Res.* **4** 870–81

[50] Yang Y, He L, Tang C, Hu P, Hong X, Yan M, Dong Y, Tian X, Wei Q and Mai L 2016 Improved conductivity and capacitance of interdigital carbon microelectrodes through integration with carbon nanotubes for micro-supercapacitors *Nano Res.* **9** 2510–9

[51] An B, Xu S, Li L, Tao J, Huang F and Geng X 2013 Carbon nanotubes coated with a nitrogen-doped carbon layer and its enhanced electrochemical capacitance *J. Mater. Chem.* A **1** 7222–8

[52] Mao N, Wang H, Sui Y, Cui Y, Pokrzywinski J, Shi J, Liu W, Chen S, Wang X and Mitlin D 2017 Extremely high-rate aqueous supercapacitor fabricated using doped carbon nanoflakes with large surface area and mesopores at near-commercial mass loading *Nano Res.* **10** 1767–83

[53] Jiang L, Wang J, Mao X, Xu X, Zhang B, Yang J, Wang Y, Zhu J and Hou S 2017 High rate performance carbon nano-cages with oxygen-containing functional groups as supercapacitor electrode materials *Carbon* **111** 207–14

[54] Sevilla M, Yu L, Zhao L, Ania C and Titiricic M 2014 Surface modification of cnts with n-doped carbon: an effective way of enhancing their performance in supercapacitors *ACS Sustain. Chem. Eng.* **2** 1049–55

[55] Wang Y, Fugetsu B, Wang Z, Gong W, Sakata I, Morimoto S, Hashimoto Y, Endo M, Dresselhaus M and Terrones M 2017 Nitrogen-doped porous carbon monoliths from polyacrylonitrile (PAN) and carbon nanotubes as electrodes for supercapacitors *Sci. Rep.* **7** 40259

[56] You B, Jiang J and Fan S 2014 Three-dimensional hierarchically porous all-carbon foams for supercapacitor *ACS Appl. Mater. Interfaces* **6** 15302–8

[57] Liu Y, Li G, Chen Z and Peng X 2017 Cnt-threaded N-doped porous carbon film as binder-free electrode for high-capacity supercapacitor and Li–S battery *J. Mater. Chem.* A **5** 9775–84

[58] Qian X, Lv Y, Li W, Xia Y and Zhao D 2011 Multiwall carbon nanotube@mesoporous carbon with core–shell configuration: a well-designed composite-structure toward electrochemical capacitor application *J. Mater. Chem.* **21** 13025–31

[59] Zhang Z, Xiao F, Qian L, Xiao J, Wang S and Liu Y 2014 Facile synthesis of 3D MnO$_2$-graphene and carbon nanotube-graphene composite networks for high-performance, flexible, all-solid-state asymmetric supercapacitors *Adv. Energy Mater.* **4** 867–72

[60] Liu Y, Li G, Guo Y, Ying Y and Peng X 2017 Flexible and binder-free hierarchical porous carbon film for supercapacitor electrodes derived from MOFs/CNT *ACS Appl. Mater. Interfaces* **9** 14043–50